Lattice strain development in an alpha titanium alloy studied using synchrotron and neutron diffraction

Kodjo Emmanuel Agbovi, Baptiste Girault, Jamal Fajoui, Saurabh Kabra, Winfried Kockelmann, Thomas Buslaps, Agnieszka Poulain, David Gloaguen

Lattice strain development in an alpha titanium alloy studied using synchrotron and neutron diffraction

Kodjo Emmanuel Agbovi[1], Baptiste Girault[1], Jamal Fajoui[1], Saurabh Kabra[2], Winfried Kockelmann[2], Thomas Buslaps[3], Agnieszka Poulain[3], David Gloaguen[1*]

[1] Research Institute in Civil and Mechanical Engineering (GeM - UMR CNRS 6183), University of Nantes, 58, rue Michel Ange - BP 420, 44606 Saint-Nazaire Cedex, France

[2] ISIS Neutron and Muon Source, Science and Technology Facilities Council, Rutherford Appleton Laboratory, Harwell, OX11 0QX, United Kingdom

[3]European Synchrotron Radiation Facility, 71 avenue des Martyrs, CS 40220, 38043 Grenoble Cedex 9, France

[*] Corresponding author: david.gloaguen@univ-nantes.fr

Abstract

Neutron and high-energy X-ray diffraction methods have been used to investigate deformation mechanisms (slip and twinning activities) during uniaxial tensile tests of Grade 1 commercially pure titanium (Ti-α). These two diffraction techniques have provided valuable and complementary information. The predictions made by an Elasto-Plastic Self-Consistent (EPSC) model, taking into account grain reorientation and stress relaxation induced by twinning activity, have been compared with the experimental data. Results clearly demonstrate that there is a good agreement between simulations and diffraction measurements. The EPSC model enables accurate predictions of: (i) the lattice strains developed in variously oriented {hk.l} grain families within the bulk material, (ii) the grain reorientation induced by twinning activity and (iii) the macroscopic stress-strain response.

Two different textured products were studied in order to evaluate the influence of texture on the mesoscopic and macroscopic responses of Ti-α alloy.

Keywords: titanium alloys, strain measurements, plasticity, modelling, anisotropy, diffraction

1. Introduction

Due to their high specific strength, good corrosion resistance and biocompatibility, titanium and its alloys are of the utmost importance for aeronautic applications and are also widely used in naval and biomedical industries [1–3]. Hexagonal Close Packed (HCP) metals present a low crystalline symmetry as compared to cubic materials. They are then governed by a heterogeneous plastic deformation, and the way it is accommodated is still not well understood. At room temperature, it is well experimentally established that prismatic slip $\{10.0\}\langle 11.0\rangle$ is the easiest deformation mode to be activated in HCP titanium. Pyramidal $\langle c+a\rangle$ slip $\{10.1\}\langle 11.3\rangle$, pyramidal $\langle a\rangle$ slip $\{10.1\}\langle 11.0\rangle$ and basal slip $\{00.2\}\langle 11.0\rangle$ are generally presented as secondary slip modes [4,5] that are more difficult to activate. In particular, $\{10.1\}\langle 11.3\rangle$ slip produces plastic deformation with a component out of the basal plane (i.e. along the $\vec{c}$-axis). Deformation along $\vec{c}$-axis can also be accommodated by twinning modes $\{10.2\}\langle 10.\bar{1}\rangle$ or $\{11.2\}\langle 11.\bar{3}\rangle$ that induce a reorientation of the crystal lattice [4,6,7]. The relative activity of these multiple deformation mechanisms strongly depends on the chemical composition, grain size, morphological and crystallographic textures, straining direction and strain rate. Understanding how the different deformation mechanisms operate during plastic deformation of titanium alloys require thus further investigations. A deeper knowledge of the mechanical behavior of HCP materials during plastic deformation calls for the use of advanced techniques such as Time-Of-Flight (TOF) neutron or High Energy synchrotron X-Ray Diffraction (HEXRD) enabling to monitor the evolution of internal elastic strains. With a high spatial resolution, X-ray synchrotron radiation allows a very small gauge

volume (200 µm × 200 µm spot size for the present study) as compared to the neutron diffraction one (4 mm × 4 mm spot size for the present study), but offers fast rate data acquisition (few seconds for synchrotron radiation and around 40 minutes for neutron diffraction in this work). This technique enables to measure online strain distributions and *in situ* during a continuous mechanical loading. In contrast, for materials characterized by a substantial creep behavior such as titanium alloys, the samples investigated by neutron techniques have to be unloaded once the desired macroscopic strain has been reached. Analyses relate thus only to the residual lattice strains remaining after a given increment of plastic deformation [8–10]. These two complementary non-destructive methods have been adopted in this work to measure the change in the {hk.l} d-spacing during tensile loadings in order to characterize the internal elastic strains (or intergranular strains) distribution. Experimental results can be explained and interpreted using a polycrystalline modeling approach like the Elasto-Plastic Self-Consistent (EPSC) model [11–15]. This micromechanical modelling is a helpful technique to characterize the mechanical state of polycrystalline materials at the grain level and to understand the role played by plastic anisotropy, slip-slip (and slip-twin) competitions in the macroscopic behavior. For example, Warwick et al. [8] have examined a textured Grade 1 Commercially Pure titanium (CP Ti) by coupling neutron diffraction to self-consistent modelling. A good agreement was found between neutron diffraction and the simulated results. The authors found that twinning produces a greater hardening than slip and that the residual lattice strains developed in the {00.2} grains are higher than in other orientations for both tensile and compression straining. A similar finding has been achieved by Gloaguen et al. [9], who analyzed the deformation mechanisms involved in the plasticity of Grade 2 CP Ti during compressive loadings. The residual lattice strain of different {hk.l} orientations was tracked in both parallel and transverse directions to the straining axis and the diffraction data were investigated to

highlight the role of tensile twin {10.2} in the α-titanium alloy. Cho et al. [10] used a similar methodology to characterize the intergranular residual strains accumulation in a near α-titanium alloy and a Ti-834 alloy during tensile tests. It has been found that it was possible to successfully reproduce the trends and magnitudes of the observed microstrains in both loading and transverse directions. The plastic behavior of a two phase titanium alloy, Ti-6Al-4V, has also been studied [16] thanks to this coupled approach. The X-ray synchrotron diffraction has likewise been used with EPSC modelling by Stapleton et al. [17] to analyze the evolution of internal lattice strains in a Ti-6Al-4V alloy during *in situ* tensile tests. A similar study has been carried out in a near β-titanium alloy [18]. The main advantage of high energy X-rays is the possibility to have short measurements during a continuous mechanical test. The number of diffracting grains is nevertheless smaller as compared to neutron diffraction experiments due to the smaller gauge volume (respectively 200 µm × 200 µm × 2 mm and 4 mm × 4 mm × 4 mm). Therefore, the lattice strains determined with synchrotron X-ray radiation are less representative due to a smaller number of crystallites contributing to the diffracting volume. The comparison with a homogenization approach is then more problematic [14].

The purpose of the work presented in this paper is to understand the internal strain development of a commercially pure titanium under uniaxial tensile loadings. Experimental observations are coupled with the predictions of the EPSC model in order to explain the plastic behavior of Ti-α and to identify the slip systems and twinning modes responsible for the plastic activity within the material. One of the objectives of this study is to evaluate the influence of crystallographic texture and twin activity on the mechanical response. An EPSC model, taking into account grain reorientation and stress relaxation induced by twinning activity, has been developed for this study. Two different textured samples (a unidirectional rolled plate and a forged bar) for the same alloy were studied in order to evaluate the influence of texture on the mesoscopic and macroscopic responses of a Grade 1 CP Ti-α alloy.

A comparison between these two techniques and the experimental internal (X-ray) and residual (neutron) strain values obtained with an EPSC model has been made to analyze the potential difference.

2. Experimental methods

2.1. Material

The investigated material is a Commercially Pure α-titanium (denoted CP Ti-α). Two samples, produced by two different forming processes, are studied: a unidirectional rolled plate and a forged bar. The samples are fully hexagonal compact phased at room temperature and their chemical compositions are given in Table 1. The tensile specimens have different geometries (see Fig. 1).

Table 1: Chemical composition data (wt.%) of the materials

Specimen	C	N	O	H	Fe	Ti
N-Sample	0.07	0.008	0.12	0.0013	-	Balance
S-Sample	0.012	0.0078	0.137	0.001	0.164	Balance

Cylindrical specimens (denoted below as N-sample) with 8 mm diameter and 42 mm gauge length were cut along the extrusion direction (represented by the Longitudinal Direction: LD, Fig. 1.a) for neutron diffraction experiments. This geometry was adopted in order to access to a sufficiently large gauge volume. However, *in situ* synchrotron experiment specimens, denoted as S-samples, have been machined along the Transverse Direction (TD) of the rolled plate, as shown on Fig. 1.b. The sample thickness was small enough (2 mm) to enable transmission measurements [19]. The metallographic characterization has revealed that the

grains are generally equiaxed with an average grain size of 40 and 45 µm in S-samples and N-samples, respectively.

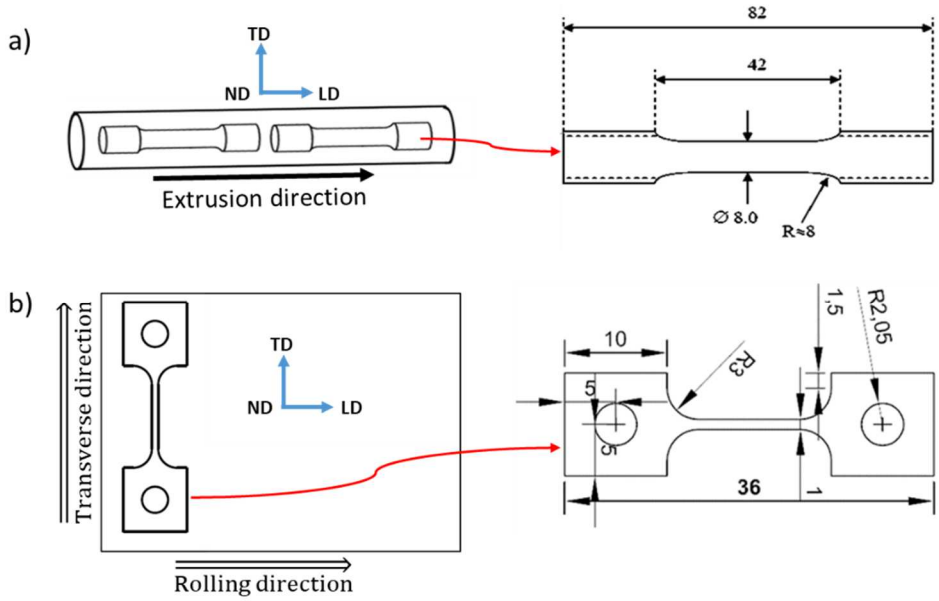

Fig. 1: Schematic view showing dimensions (in mm) of the samples used in a) neutron and b) synchrotron experiments. LD: Longitudinal (loading) Direction, TD: Transverse Direction, ND: Normal Direction

N-sample texture measurements were performed on the GEM beamline at the ISIS neutron spallation source (United Kingdom). Information about the instrument and the measurement technique can be found in [20,21]. Measurements of the initial texture (Fig. 2.a) have revealed that the samples have a strong asymmetric texture in the TD-ND plane, perpendicular to the loading axis (LD). This texture is consistent with the analyses made on extruded hexagonal polycrystalline samples found in literature [8,9,22].

The S-sample initial texture, shown in (Fig. 2.b), was measured using the neutron diffraction on the 6T1 diffractometer from the French national Orpheus nuclear reactor (at Léon Brillouin Laboratory, Saclay, Gif-sur-Yvette, France). As revealed in Fig. 2.b, basal poles are tilted +

30° away from the Normal Direction axis (corresponding to the plate normal direction) toward the Transverse Direction. The observed texture is typical of rolled titanium plates followed by recrystallization.

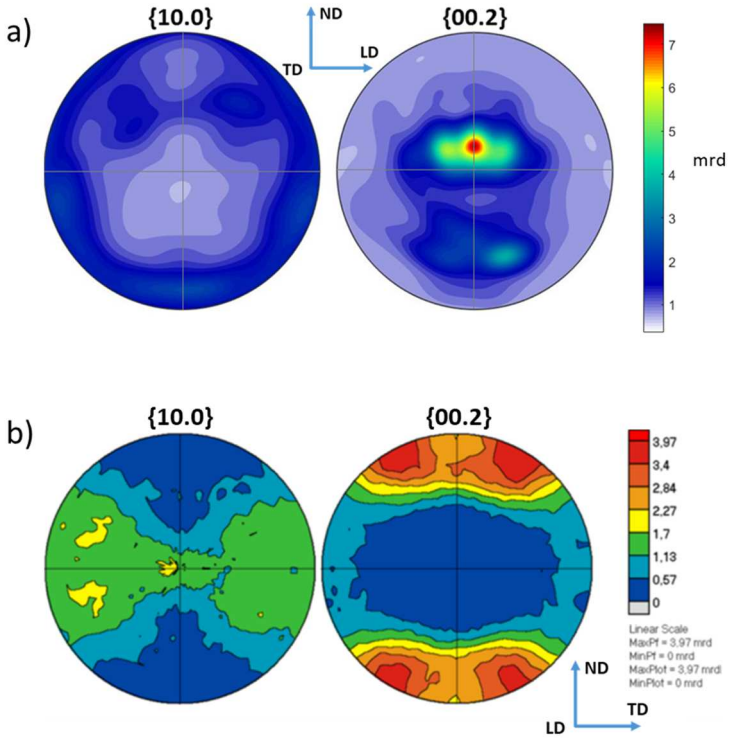

Fig. 2: Initial crystallographic textures of the studied specimens a) N-sample and b) S-sample

2.2. *Neutron diffraction measurements*

Tensile tests were performed at room temperature using the ENGIN-X neutron diffractometer (Fig. 3) at the ISIS spallation neutron source. The measurement steps were applied by a 50 kN Instron testing machine with a strain rate of $10^{-5}\ s^{-1}$ up to 6 % of macroscopic strain. The specimen was subjected to a displacement controlled regime. The incident slits and radial collimators defined a scattering volume of $4 \times 4 \times 4$ mm^3 with a counting time of 43 minutes per measurement. The macroscopic strain was determined using an extensometer that spanned the irradiated region. The sample was first deformed to the desired macroscopic strain and

149 then immediately unloaded, as shown in Fig. 4, to avoid any strain relaxation due to the creep
150 behavior.

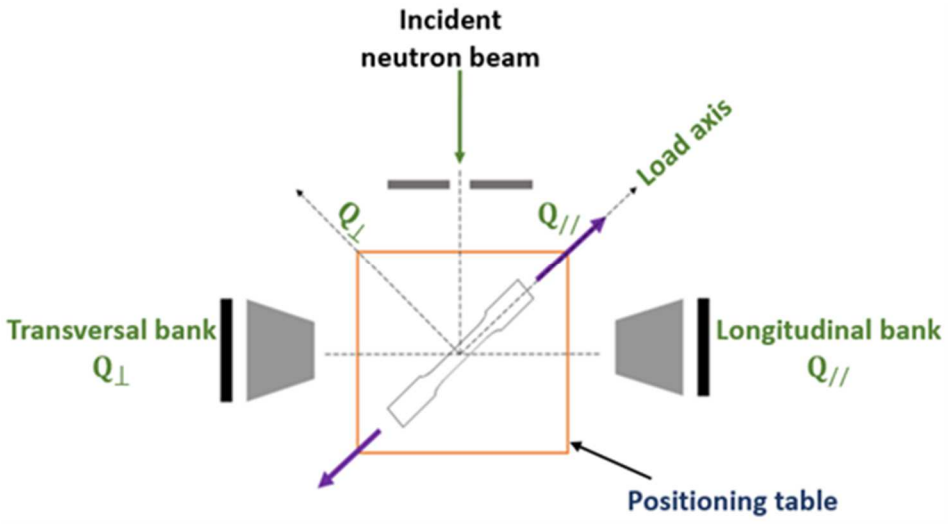

151

152 **Fig. 3:** Schematic top-view of the set-up used on the neutron diffraction instrument ENGIN-X

153

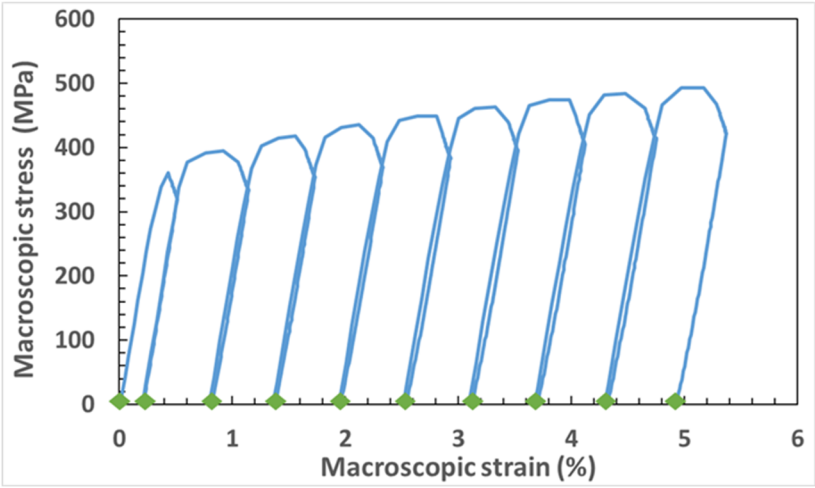

154

155 **Fig. 4:** Measured macroscopic stress– strain curve obtained with ENGIN-X. The green points
156 indicate the macroscopic strain during neutron measurements after unloading, i.e. at zero
157 applied load.

158 Successive steps have been achieved at room temperature, in the plastic regime, studying the
159 remaining residual strains resulting from a given increment of plastic deformation at zero

applied load. The schematic view of the ENGIN-X instrument (Fig. 3) shows a horizontal loading axis positioned at 45° with respect to the incident beam. Two detector banks are set up horizontally at ± 90° from the incident beam, enabling simultaneous measurements of lattice strains from {hk.l} plane families with parallel (i.e. along the loading direction) and perpendicular (i.e. along the transverse direction) directions, as regard to the loading applied direction (Fig. 3). The Time-Of-Flight (TOF) technique enables to collect simultaneously an entire diffraction pattern (the effective d-spacing range from 0.88 to 2.63 Å) on each detector [23]. Single peak fitting was performed using the Open Genie code [24] with Gaussian functions. The lattice strain $\langle \varepsilon(hk.l,\varphi,\psi)\rangle_{V_d}$ of a grain group having a common {hk.l} plane-normal parallel to the diffraction vector $\vec{Q}$ (defined by azimuthal and inclination angles, respectively φ and ψ) can be calculated by the following formula:

$$\langle \varepsilon(hk.l,\varphi,\psi)\rangle_{V_d} = ln\left(\frac{\langle d(hk.l,\varphi,\psi)\rangle_{V_d}}{d_0(hk.l)}\right) \qquad \textit{Eq. 1}$$

The initial lattice parameter $d_0(hk.l)$, measured before deformation of the material, is used as the reference point for this calculation. $\langle X\rangle_{V_d}$ (V_d: diffracting volume, $X = \varepsilon(hk.l,\varphi,\psi)$ *or* $d(hk.l,\varphi,\psi)$) stands for the averaging over the diffracting grains for the considered {hk.l} reflection. $\langle d(hk.l,\varphi,\psi)\rangle_{V_d}$ is the measured lattice spacing and resulting lattice strain values are given as micro-strain (denote με, i.e. units of 10^{-6}). In the remainder of the paper, // and ⊥ symbols respectively refer to the lattice strain in the parallel and perpendicular directions to the stress axis (corresponding to the extrusion direction).

2.3. Synchrotron X-ray measurements

ID15B beamline at the ESRF (the European Synchrotron Radiation Facility, Grenoble, France) has been used to perform *in situ* tensile tests in a transmission mode, with a monochromatic X-ray radiation of 87 keV (λ = 0.1425 Å wavelength). The configuration of

the experimental setup is shown in Fig. 5.a. The tests were performed on an Instron 8800 electrothermomechanical test machine with a maximum load capacity of 3 kN under a constant strain rate $4.10^{-4}\,s^{-1}$ up to 4 % macroscopic strain. The load was applied perpendicular to the rolling direction (Fig. 1.b). Fig. 6 shows the macroscopic curve obtained on ID15B beamline.

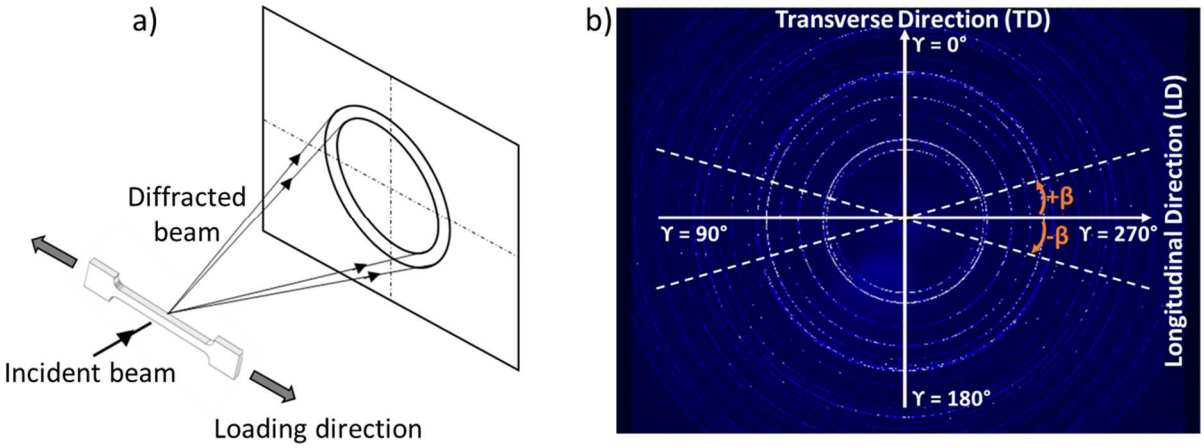

Fig. 5: a) Experimental setup showing S-sample positioning, b) example of image recorded on the 2D detector with γ and β angle definitions

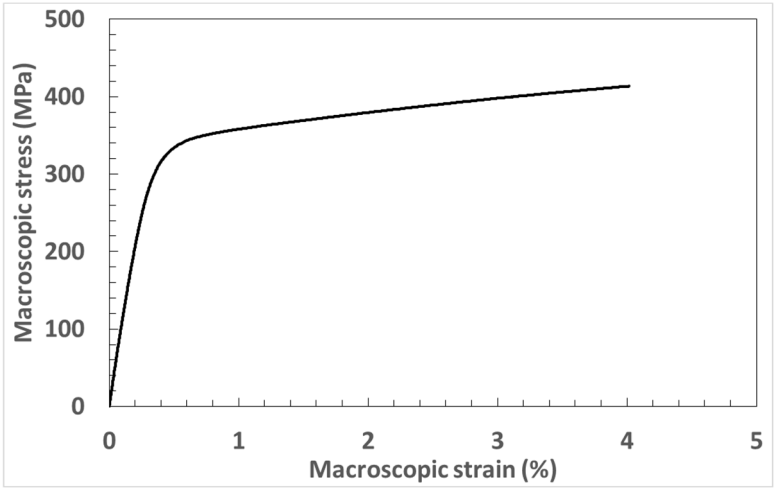

Fig. 6: Measured macroscopic stress – strain curve obtained on the ID15B beamline.

The diffraction patterns (example presented in Fig. 5.b), have been recorded using a 2D Pixium 4700 flat-panel detector [25], positioned in agreement with the targeted {hk.l} diffracting planes and signal optimization. Each ring recorded with the 2D detector corresponds to a {hk.l} crystallographic family plane. Regarding high α-Ti creep rates, high speed data acquisition is mandatory for online measurements (2s counting time every 7s). Considering the sample dimensions (1 mm × 2 mm) and the beam size (200 µm × 200 µm), the irradiated volume is 0.2 × 0.2 × 2 mm^3. It has to be underlined that this latter volume is much smaller than the gauge volume obtained in neutron diffraction experiments (4 × 4 × 4 mm^3). The recorded images were processed using the FIT2D pattern analysis software [26], which integrates the two-dimensional images (Fig. 5.b) into one-dimensional spectra (intensity $I(\gamma, hk.l)$ vs. scattering angle $\langle 2\theta(hk.l)\rangle_{V_d}$). ($\langle d(hk.l)\rangle_{V_d}$, $I(\gamma, hk.l)$) couples have been calculated integrating the 2D patterns over a given ± β range for the two directions : longitudinal (i.e. LD, corresponding to the symmetrical azimuth angles γ = 90 and 270°) and transverse (i.e. TD, corresponding to γ = 0 and 180°). The integration range over the ring (defined by ± β) has to be reasonably large for a statistically representative behavior of the material according to the considered orientation i.e. sufficient amount of the diffractive crystallites contributing to the signal. In addition, the β value must be small enough to cover only crystallites oriented relatively to the considered direction. For these reasons and based on [14,19] studies, the intensities of the diffraction rings were integrated, as a compromise, within "cake shape" sectors defined by β ± 10°. Finally the arithmetic mean values of the d-spacings $\langle d(hk.l)\rangle_{V_d}$ were calculated from the averaging of the symmetrically equivalent γ and γ + 180° angles.

The $\langle 2\theta(hk.l)\rangle_{V_d}$ positions of the diffraction peaks were determined using pseudo-Voigt function fitting [27–29]. The lattice spacing $\langle d(hk.l)\rangle_{V_d}$ was then calculated from the peak positions using the Bragg's law [30].

2.4. Twinning activity in both N-sample and S-sample

Fig. 7.a shows the initial N-sample texture measured on the GEM beamline. The specimen has a strong asymmetric texture in the TD-ND plane with the majority of grains with their basal normal close to the transverse direction and perpendicular to the loading axis. After 6 % of macroscopic deformation, a reorientation of the {00.2} poles was observed (presented by a white framed area in Fig. 7.b). This can be associated with twinning deformation. Actually, the activation of compression twinning $\{11.2\}\langle 11.\bar{3}\rangle$ produces a reorientation of the basal poles of approximatively 65° [6,31].

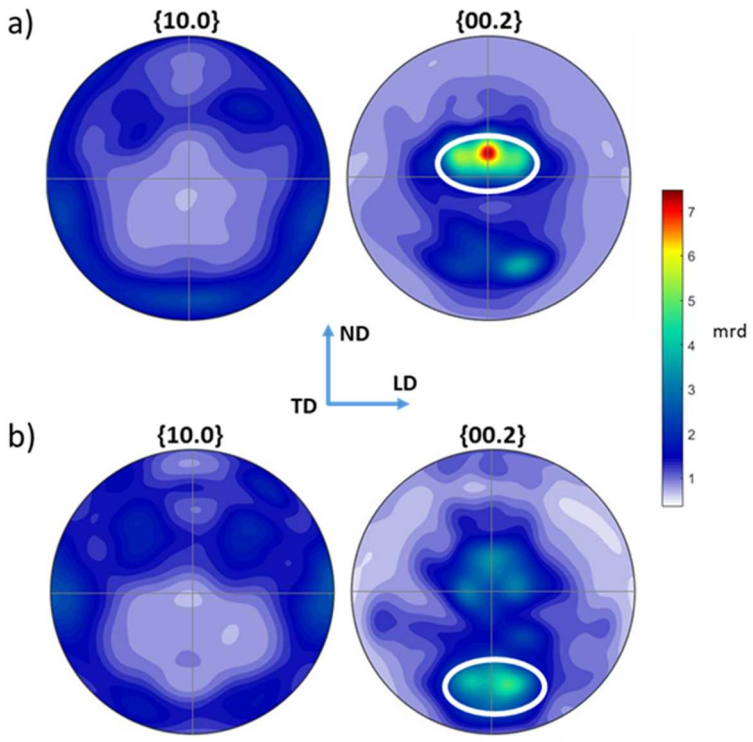

Fig. 7: Experimental {10.0} and {00.2} pole figures of the a) as-received N-sample and b) after the tensile loading up to 6 %. Pole figures (PFs) show the ND–LD plane, the center of the poles being the TD.

Tensile loading along the longitudinal (or extrusion) direction, with the $\vec{c}$-axis close to the transverse direction (Fig. 7.a), reorients the $\vec{c}$-axis of the grains undergoing twinning deformation. The twinned area fraction can be quantitatively calculated focusing on the difference between {00.2} pole figures of both as-received and deformed samples. Based on the work of Brown et al. [32] and integrating over the white framed area in Fig. 7.a, the total twin volume fraction after 6 % applied macroscopic strain is about 13 %.

Contrary to the previous analysis, crystallographic texture of the S-sample could not be measured in synchrotron experiments after the tensile test. Thus, analysis has focused on the evolution of the intensity measured during *in situ* straining as shown in Fig. 8. Gharghouri et al. [33] were the first to show that severe intensity variations during plastic deformation can be reliably attributed to twinning activity. Hence, Muránsky et al. [12], Brown et al. [32] and Gharghouri et al. [33] highlighted a direct correlation between the intensity evolution of {10.0} and {00.2} diffraction peaks, measured with detectors placed at 90° from each other and the tensile twinning $\{10.2\}\langle 10.\bar{1}\rangle$ that reorients the twin grains by 90° [31]. Our study confirms findings of these authors: a dramatic increase in {10.0} intensity in the loading direction (LD) is observed above around 365 MPa macroscopic stress (Fig. 8.a). At the same time, in the transverse direction (TD), the intensity of the {10.0}-orientated grains decreases, while the {00.2} peak intensity increases significantly (Fig. 8.b). This reflects a change in the grain volume fraction that diffracts in the TD and LD. Owing to the texture of the as-received S-sample, the changes of {00.2} and {10.0} peak intensities in these two directions are due to tensile twinning $\{10.2\}\langle 10.\bar{1}\rangle$ activity.

The evolution of the intensity of others reflections such as {10.1} in TD (Fig. 8.b) could naturally also be related to other twining mode activity but it is difficult to discern which one only in the light of the information given by present synchrotron X-ray diffraction experiments.

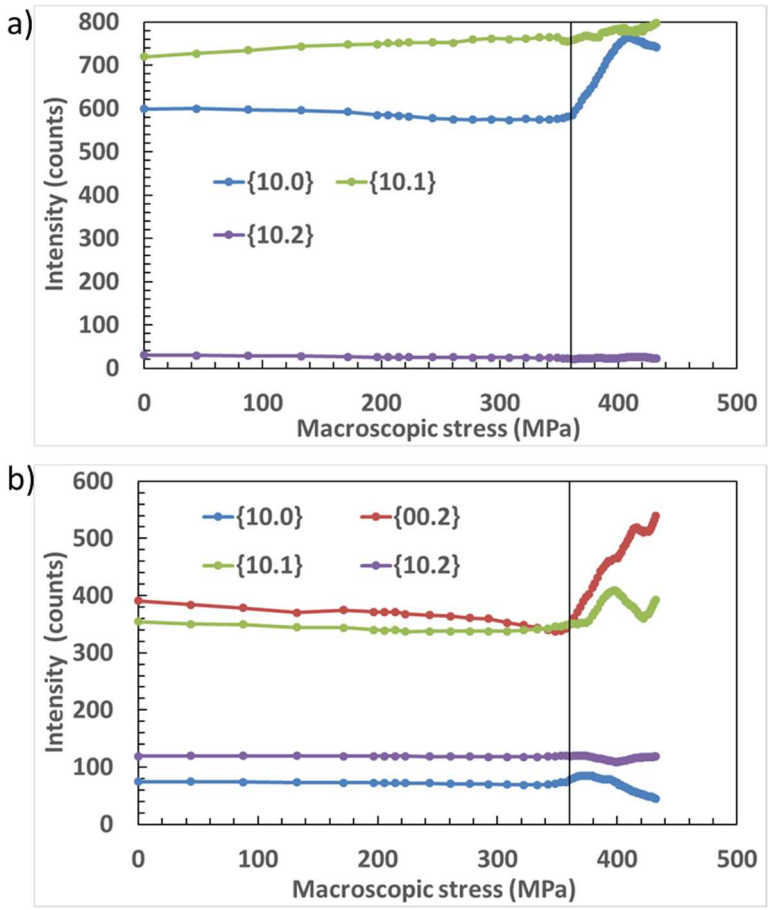

Fig. 8: Evolution of the diffraction peak intensities (Miller indices indicated in the plot) obtained from *in situ* synchrotron X-ray diffraction measurements in the a) loading (LD) and transverse (TD) directions

3. Twinning scheme for Elasto-Plastic Self-Consistent model

The one-site EPSC approach applied in this work incorporate the single crystal plasticity model derived by the pioneering works of Kröner [34,35] and Hill [36]. It adopts a weighted population of grains approach which exploits the experimentally measured crystallographic

textures as inputs. Each grain is assumed to have the form of an ellipsoidal inclusion embedded in a homogeneous effective medium with anisotropic properties representative of the textured polycrystalline aggregate. The model has been extensively described in [9,15,37], therefore only a brief description will be given here. More information concerning the approach used can also be found in [38–41]. This model enables to incorporate the measured experimental results as well as to determine the strain hardening parameters, the related Critical Resolved Shear Stress (CRSS) and the mechanical strain/stress state at the mesoscopic level, for the diffracting volume and during the mechanical tests.

The slip rate $\dot{\gamma}^{g}$ on a slip system g is linked to the resolved shear stress rate $\dot{\tau}^{g}$ [40,41] by:

$$\dot{\gamma}^{g} = T^{g}(\tau^{g}, \tau_{c}^{g}, \dot{\tau}^{g})\dot{\tau}^{g} \qquad \textit{Eq. 2}$$

where τ^{g} is the resolved shear stress and τ_{c}^{g}, the critical resolved shear stress. T^{g} is the deformation mechanisms management function and is expressed by:

$$T^{g} = \frac{1}{H^{gg}}\left(\frac{1}{2}(1 + tanh(\tau^{g}))\right)\left(\frac{1}{2}\left(1 + tanh\left(k\left(\frac{\tau^{g}}{\tau_{c}^{g}} - 1\right)\right)\right)\right)\left(\frac{1}{2}(1 + tanh(\dot{\tau}^{g}))\right) \qquad \textit{Eq. 3}$$

where H^{gg} is the self-hardening coefficient and k, a numerical parameter. The hyperbolic tangent function was used because it enables the mechanical and hardening behaviors, observed in practice, to be reproduced [40,41].

The hardening matrix H^{gr} is introduced to describe the CRSS rate evolution in a system g, as a function of the plastic slip (or twinning) on the other deformation systems r:

$$\dot{\tau}_{c}^{g} = \sum_{r} H^{gr}\dot{\gamma}^{r} \qquad \textit{Eq. 4}$$

where $\dot{\tau}_{c}^{g}$ is the CRSS rate. Due to a lack of relevant experimental data on latent hardening nature, especially in titanium alloys, the interactions between the different deformation modes are described by a simple law. In the present work, the hardening matrix is described by the following equation [39]:

$$H^{gr} = q.H^{gg} \qquad \text{Eq. 5}$$

H^{gg} is the self-hardening coefficient and H^{gr} corresponds to the latent hardening when g slip system is different from r. The q factor defines the degree of latent hardening.

In the present study, twinning deformation is treated as a directional slip mechanism [42–44]. It is characterized by the normal to the twinning plane n^t and the twinning direction m^t. When a twinning system becomes active, a part of the parent grain is reoriented and stress relaxation is introduced. In order to take into account these phenomena, different algorithms have been proposed. Van Houtte [45] was the first to propose a "Monte Carlo" approach consisting of randomly sampling and reorienting full grains. A scheme of such an approach has been proposed by Tomé et al. [46]: reorienting the grain according to the most active twinning system, named Predominant Twin Reorientation (PTR) formulation. Lebensohn and Tomé [47] have proposed another one called a Volume Fraction Transfer (VFT) formulation. The Euler space is partitioned in cells and, instead of keeping the grain volume fraction constant while changing its orientation, as done in PTR, the volume fraction assigned to each cell evolves with deformation. This last approach enables to predict the crystallographic texture evolution but it has the disadvantage of losing the grain identity and it does not allow to implement a realistic hardening scheme.

The scheme proposed in this paper, called Modified Predominant Twin Reorientation (M-PTR), is based on Tomé et al. [46] and Clausen et al. [48] assumptions.

3. 1 Modified Predominant Twin Reorientation (M-PTR)

The M-PTR scheme accounts for: (i) the stress relaxation associated with the twin formation and, (ii) the twinning fraction effect on texture evolution. At each imposed strain increment, the philosophy of the PTR scheme is adopted. The accumulated shear of each twin system in

each grain is recorded and the Predominant Twin System (PTS) is identified as the one that involves the maximum volume fraction f_{cum}^{t} (Eq. 6):

$$f_{cum}^{t} = \sum \frac{\dot{\gamma}^{t}}{S^{t}} \qquad \textit{Eq. 6}$$

Here, $\dot{\gamma}^{t}$ represents the shear due to the twin system t and S^{t} is the characteristic twinning shear.

Once the predominant twin system is identified, the total fraction f_{cum}^{gr} accumulated in each grain is given by the sum over all N^{t} active twin systems:

$$f_{cum}^{gr} = \sum_{t=1}^{N^{t}} f_{cum}^{t} \qquad \textit{Eq. 7}$$

In the EPSC model, a threshold fraction f_{limit} is introduced in Eq. 8. The idea behind this parameter is to take into account the twinning nucleation mechanism and the initial growth process in the parent grain. More information about these phenomena can be found in [49–52]. When the volume fraction f_{cum}^{gr} in a parent grain reaches the threshold f_{limit}, that fulfills the following equation (Eq. 8), the PTS system is selected and the corresponding grain is fully reoriented.

$$f_{cum}^{gr} \geq f_{limit} \qquad \textit{Eq. 8}$$

f_{limit} is the model parameter that will be adjusted. Based on Tomé et al. [46], Tomé and Lebensohn [53] and Wronski et al [54] studies, the threshold value f_{limit} is taken between 5 and 50 %. If Ω^{m} is the parent grain orientation, the twin orientation (child) Ω^{tw} will be determined by the relation (Eq. 9) [55,56]:

$$\Omega^{tw} = R^{tw}\,\Omega^{m} \qquad \textit{Eq. 9}$$

The lattice rotation tensor R^{tw} is given by:

$$R^{tw} = 2n^{t} \otimes n^{t} - I \qquad \textit{Eq. 10}$$

where n^{t} is the twinning plane normal and I is the unit tensor.

Due to the fact that the twinning deformation is a secondary deformation mechanism in our study (see section 2), the nucleated twin is treated as a new independent grain and the new orientation is kept constant until the end of the simulation.

3.1. 1 Twin variant selection criterion

Experimental studies have shown that each active twin system has six possible variants. Therefore, it is important to define a criterion allowing for the selection of the most appropriate twinning variant. Electron Backscatter Diffraction (EBSD) statistical analyses on zirconium [50] showed that {10.2} twinning variants with the highest Schmid factors were the most active (about 56-60 % activation probability). Similar dependencies were observed for {10.2} and {11.2} twinning systems during tensile or compressive loading of commercially pure titanium in [54,57,58]. However, it has been noticed that variants with lower Schmid factors may also contribute to plastic deformation. Thereby, it is clear that the selection process is crucial since it affects the microstructure and the texture evolution of the sample. For example, Wronski et al [54] have used a Visco-Plastic Self-Consistent (VPSC) model with a simple Monte Carlo twin variant selection criterion to predict with accuracy the crystallographic texture evolution in titanium during tensile and compression tests. On the basis of these analyses and in order to provide a reasonable description of the selection process, one variant is picked randomly among the three with the highest twin fractions. The goal behind is to allow for the relatively less predominant variants to accommodate plastic deformation.

3.1. 2 Estimation of the stress relaxation

As mentioned previously, twinning activity induces not only the twinned zone reorientation but also a stress relaxation in the parent grain [48,59,60]. Stress relaxation has been implemented on the assumptions made in [48,59,60]. Elastic strain and stress, originally

present and developed in the new formed (child) grain are estimated by applying continuity equations for tractions and displacements across the twin boundary. The stress and strain at the grain level are assumed to be uniform in the present model and the elastic strains within the plane of the child twin are supposed to be compatible to the matrix on the other side of the twin boundary as described in [48]. Furthermore, stresses acting on the twining plane are also assumed to be equal across the twin interface. When the newly child grain is created and grown to an accumulated twin volume fraction f_{cum}^{t} (given in Eq. 6) of the parent grain, a shear strain γ^{t} for the twin system *t* is calculated from the equation below:

$$\gamma^{t} = f_{cum}^{t}\, S^{t} \qquad \textit{Eq. 11}$$

The plastic shear γ^{t} generates necessarily a back-stress between the parent and child grains in order to accommodate the plastic deformation. It is determined thanks to the Eq. 12 assuming that the imposed plastic shear is equal and opposite to the elastic shear:

$$\varepsilon^{II\,0} = -\,R^{t}\,\gamma^{t} \qquad \textit{Eq. 12}$$

Here, $\varepsilon^{II\,0}$ represents the elastic back-strain and R^{t}, the Schmid tensor for the twin system *t*. According to Clausen et al. [48], parent crystal is assumed to be infinitely stiff in comparison with the newly formed twin. It is thus not accommodating any of the plastic shear, forcing the twin to develop an equal and opposite elastic strain. The back-stress is computed with the following relation (Eq. 12), using the twin elastic stiffness tensor:

$$\sigma^{II\,0} = c^{t}\,\varepsilon^{II\,0} \qquad \textit{Eq. 13}$$

In the formulation applied, the parent and the twin child single-crystal elastic coefficients are supposed to be the same. Then, the stress relaxation is introduced by correcting the current stress with the calculated back-stress $\sigma^{II\,0}$. The sum is made over the twin systems *t* which become active in the current step [48,60]:

$$\sigma^{II} = \frac{\sigma^{II} + \sum_{t}\,\sigma^{II\,0} f_{cum}^{t}}{1 - \sum_{t} f_{cum}^{t}} \qquad \textit{Eq. 14}$$

3. 2 Model parameter determination

In order to perform the numerical simulations, the model parameters must be identified to describe simultaneously the macroscopic stress-train curve and the lattice strains measured on the various {hk.l} reflections. The single crystal elastic constants used in these simulations are shown in Table 2.

Table 2: The single crystal elastic constants (GPa) used in M-PTR model

Reference	c_{11}	c_{12}	c_{13}	c_{33}	c_{44}	c_{66}
[61]	162.4	92	69	180.4	46.7	35.2

Experimental PFs were used to generate the Orientation Distribution Function (ODF). A set of 2000 grain orientations weighted by the measured volume fraction has been selected from the experimental ODF. The choice of this number is the result of a preliminary study that allows us to determine the sufficient numbers of grains which describe correctly the experimental data (i.e. neutron or synchrotron measurements) [9,11]. On the basis of experimental observations in [4,7,62,63], the deformation systems considered in the simulations are: prismatic slip (denoted P⟨a⟩), basal (B⟨a⟩), pyramidal ($\Pi_1\langle a\rangle$), first-order pyramidal ($\Pi_1\langle c+a\rangle$) and {11.2} twinning (ctw-{11.2}) for neutron data simulations and, prismatic slip (P⟨a⟩), basal (B⟨a⟩), pyramidal ($\Pi_1\langle a\rangle$), first-order pyramidal ($\Pi_1\langle c+a\rangle$), {10.2} twinning (ttw-{10.2}) and {11.2} twinning (ctw-{11.2}) for X-ray synchrotron data simulations. In the two cases, the optimal value assigned to the parameter k (see Eq. 3) is 20. This is to ensure the stability and numerical convergence of the simulations [40,41].

As previously pointed out, owing to a lack of relevant data on the nature of latent hardening in HCP titanium alloys and to be more consistent with the theoretical and experimental information currently available, a simple and empirical law in Eq. 5 is applied to describe the interactions between different deformation modes. The q parameter (see Eq. 5), which

391 determines the degree of latent hardening has been adjusted to provide the best accordance
392 between the experimental and predicted results (set to a value of 1.3 for the simulations).
393 Concerning the twinning activity, the threshold fraction f_{limit} is set to 25 % what leads to a
394 good description of the material behavior.
395 Due to the easy activation of prismatic deformation mode P⟨a⟩, its CRSS value $\tau^{P\langle a\rangle}$ is
396 directly related to the macroscopic yield strength and the elastic-plastic transition during
397 tensile tests. The self-hardening coefficient $H^{P\langle a\rangle}$ was determined by fitting experimental
398 macroscopic stress-strain curves at the plasticity activity outset. These parameters are then
399 adjusted comparing neutron and synchrotron diffraction measurements. About basal (B⟨a⟩),
400 pyramidal ($\Pi_1\langle a\rangle$), first-order pyramidal ($\Pi_1\langle c+a\rangle$), {10.2} twinning (ttw-{10.2}) and
401 {11.2} twinning (ctw-{11.2}), there is less consensus on their relative role on the overall
402 behavior. These deformation mechanisms activation sequence can be found in the literature
403 and may differ from one type of alloy to another and / or from one author to another [64–68].
404 The main goal here is to identify a set of parameters able to explain the results obtained at
405 both the macroscopic scale and diffracting volume level. Several numerical simulations are
406 performed to determine the right set of parameters, in a first step, to successively favor in turn
407 one or several mechanisms. Fig. 9.a shows an example of comparison of the simulated results
408 for {20.1} reflection with different activation sequence combinations (denoted COMB1,
409 COMB2, COMB3 and COMB4) and the measured residual lattice strain in neutron
410 diffraction. A qualitative analysis shows that only COMB2 sequence reproduces correctly the
411 behavior of {20.1} grain groups. This illustrates clearly the influence of the choice of the
412 number of deformation modes and their hierarchy on the mechanical behavior at the
413 diffracting volume level, even if all these combinations describe the observed macroscopic
414 behavior (Fig. 9.b).

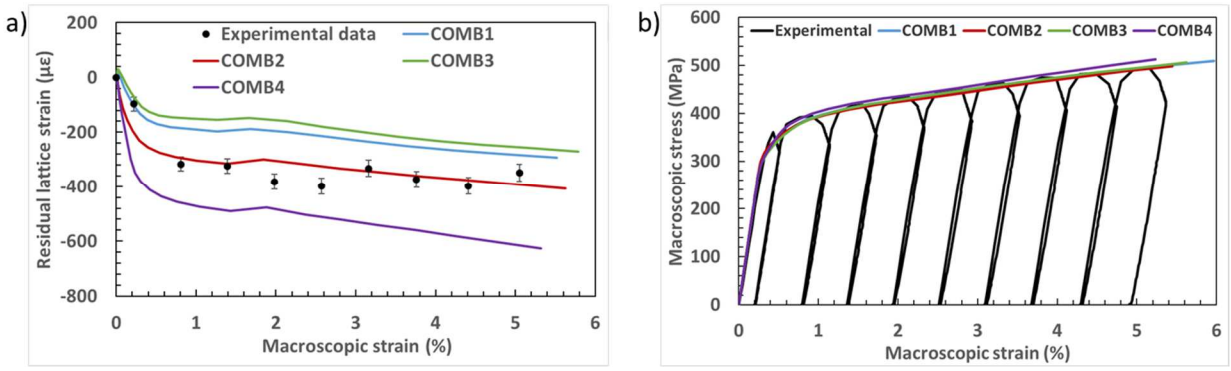

Fig. 9: a) Residual experimental (symbols) and predicted (lines) lattice strain evolution of {20.1} grains in loading direction versus applied stress and b) Experimental and simulated macroscopic stress–strain curves during neutron diffraction experiments. COMB1: $\mathbf{P\langle a\rangle}$ - $\mathbf{B\langle a\rangle}$ - $\Pi_1\mathbf{\langle a\rangle}$ - $\Pi_1\mathbf{\langle c+a\rangle}$ - **ctw**-$\{\mathbf{11.2}\}$, COMB2: $\mathbf{P\langle a\rangle}$ - $\Pi_1\mathbf{\langle a\rangle}$ - $\mathbf{B\langle a\rangle}$ - $\Pi_1\mathbf{\langle c+a\rangle}$ - **ctw**-$\{\mathbf{11.2}\}$, COMB3: $\mathbf{P\langle a\rangle}$ - $\mathbf{B\langle a\rangle}$ - $\Pi_1\mathbf{\langle c+a\rangle}$ - **ctw**-$\{\mathbf{11.2}\}$ and COMB4: $\mathbf{P\langle a\rangle}$ - $\Pi_1\mathbf{\langle a\rangle}$ - $\Pi_1\mathbf{\langle c+a\rangle}$ - **ctw**-$\{\mathbf{11.2}\}$

In order to obtain the final material parameters from neutron strain measurements, a least squares method is used, in a second step, to optimize the parameters by minimizing a function e^2 defined as the sum of squares between deviations of the experimental and simulated quantities, over all p grain groups:

$$e^2 = \sum_{i=1}^{p}\left(\frac{\langle\varepsilon(hk.l,\varphi,\psi)\rangle^i_{V_d\,meas} - \langle\varepsilon(hk.l,\varphi,\psi)\rangle^i_{V_d\,simul}}{u\left(\langle\varepsilon(hk.l,\varphi,\psi)\rangle^i_{V_d\,meas}\right)}\right)^2 \qquad \textit{Eq. 15}$$

where $\langle\varepsilon(hk.l,\varphi,\psi)\rangle^i_{V_d\,meas}$ is the measured value, $\langle\varepsilon(hk.l,\varphi,\psi)\rangle^i_{V_d\,simul}$ the simulated value, and $u\left(\langle\varepsilon(hk.l,\varphi,\psi)\rangle^i_{V_d\,meas}\right)$ the uncertainties of the measured lattice strains.

The final set of values that gives the optimum agreement between the measured and simulated results are summarized in Table 3.

Table 3: Optimized set of CRSS and hardening coefficients (MPa) obtained with the model. In blue, CRSS normalized values with respect to $CRSS^{\mathbf{P\langle a\rangle}}$, determined with the EPSC model and neutron diffraction results.

	Neutron diffraction		Synchrotron diffraction	
	CRSS	**H^{gg}**	**CRSS**	**H^{gg}**
$\mathbf{P\langle a\rangle}$	115 (1)	120	110 (1)	100
$\mathbf{B\langle a\rangle}$	150 (1.30)	180	150 (1.36)	150
$\mathbf{\Pi_1\langle a\rangle}$	130 (1.13)	140	120 (1.09)	120
$\mathbf{\Pi_1\langle c+a\rangle}$	240 (2.09)	250	180 (1.64)	200
$\mathbf{ttw\text{-}\{10.2\}}$	-	-	190 (1.73)	250
$\mathbf{ctw\text{-}\{11.2\}}$	250 (2.17)	300	220 (2)	300

4. Model results and discussion

Before starting the simulations, residual stresses were quantified in the as-received N-sample and S-sample.

Lattice parameters a = 2.9509 Å and c = 4.6844 Å of the N-sample were found from a Rietveld refinement [10] of the initial entire diffraction ring for measurements along the LD. From these, the ideal d-spacing $\langle d_0^{Rietveld}(hk.l)\rangle_{V_d}$ for all peaks {hk.l} can be calculated from:

$$\frac{1}{\langle d_0^{Rietveld}(hk.l)\rangle_{V_d}} = \frac{4h^2+hk+k^2}{3a^2} + \frac{l^2}{c^2} \qquad \textit{Eq. 16}$$

The difference between the predicted $\langle d_0^{Rietveld}(hk.l)\rangle_{V_d}$ and measured d-spacing $\langle d(hk.l,\varphi,\psi)\rangle_{V_d}$ by neutron diffraction is assumed to be due to initial residual lattice strain $\varepsilon_{hk.l}^{res}$ $\left(\varepsilon_{hk.l}^{res} = \frac{\langle d_0^{Rietveld}(hk.l)\rangle_{V_d}}{\langle d(hk.l,\varphi,\psi)\rangle_{V_d}} - 1\right)$ in the extrusion direction (see Table 4).

444

445 **Table 4:** Initial residual lattice strains in N-sample in the extrusion direction (LD)

{hk.l}	**{10.0}**	**{00.2}**	**{10.1}**	**{10.2}**
$\boldsymbol{\varepsilon^{res}_{hk.l}}$ **(×10^{-6})**	91 ± 38	22 ± 50	-57 ± 40	-62 ± 46
{hk.l}	**{11.0}**	**{10.3}**	**{11.2}**	**{20.1}**
$\boldsymbol{\varepsilon^{res}_{hk.l}}$ **(×10^{-6})**	-40 ± 38	64 ± 48	-55 ± 42	-116 ± 39

446

447 Similar order of magnitude is also found along TD. This indicates that the maximum
448 deviation is equivalent to a strain of 120 × 10^{-6}, and thus corresponds to initial residual
449 stresses below 10 MPa.
450 The as-received cold rolled sheet used in this study has already been studied in previous work
451 [15]. Analysis of the residual stress obtained from {30.2} and {21.3} reflections have then
452 shown values between -10 ± 35 MPa and +12 ± 24 MPa along the rolling direction. The stress
453 values along the TD are also in the same order of magnitude. Eventually, the two samples N
454 and S display rather low residual stress values and latter do not play, *a priori*, a significant
455 role on the elastoplastic behavior. For this reason, initial residual strains / stresses in the as-
456 received material were not accounted for in the model.

457 *4. 1 Neutron diffraction results*

458 The EPSC model developed in the section 3 is used here to simulate the mechanical behavior
459 of the CP Ti-α alloy. Experimental and predicted macroscopic responses of the N-sample
460 under uniaxial tensile test along the extrusion direction (or LD) is shown Fig. 10.a.
461 The plastic slope predicted by the model is in good agreement with that measured up to 5 %
462 macroscopic strain. The calculated value of the Young's modulus of 107 GPa is close to the

experimental one equal 102 ± 1 GPa. This is consistent with the values commonly found in the literature [69].

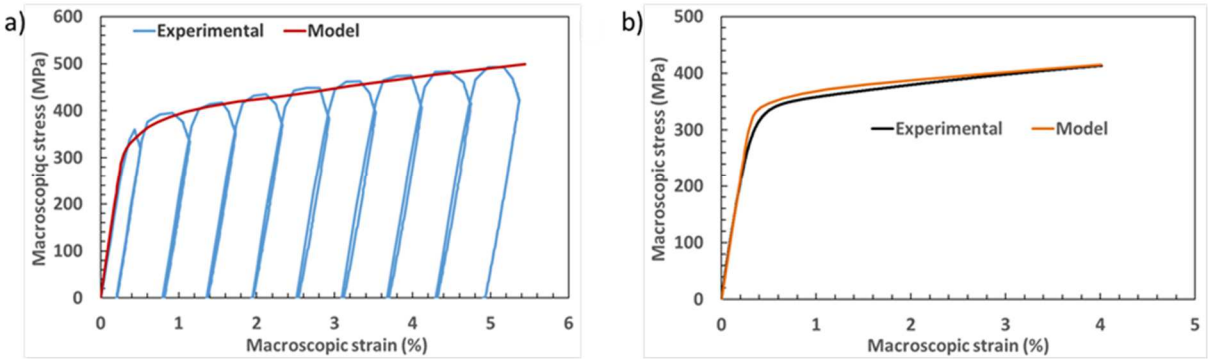

Fig. 10: Experimental and simulated macroscopic stress–strain curves in a) neutron and b) synchrotron diffraction experiments

Fig. 11 shows the predicted relative activity of each deformation mode considered in the simulation. The experimental macroscopic yield stress is about 280 MPa corresponding to 0.29 % total strain. The adjusted CRSS values are consistent with the EBSD analyses of Barkia et al. [67] with the following order: P⟨a⟩ - Π_1⟨a⟩ - B⟨a⟩ - Π_1⟨c + a⟩ - ctw-{11.2}.

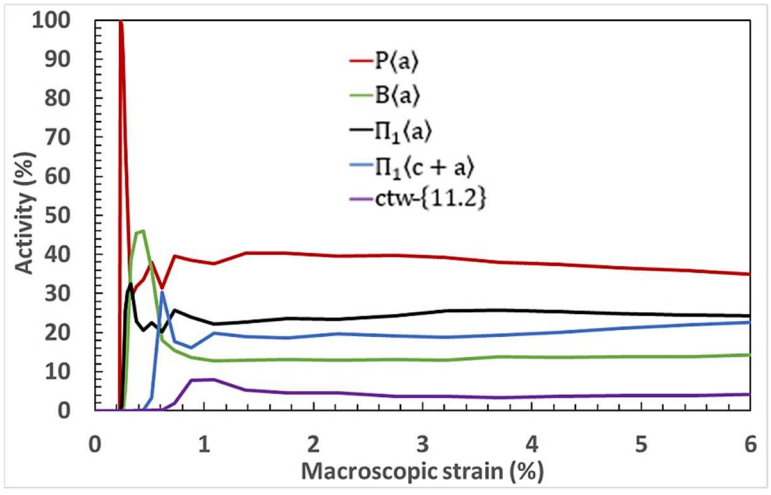

Fig. 11: Relative contribution of each deformation mode to the total plastic deformation as a function of deformation during neutron diffraction experiments

The main deformation mode is prismatic slip. For example, at 3 % macroscopic total strain, the proportions of activated systems are: 39 % for prismatic slip, 13 % for basal slip, 25 % for pyramidal ⟨a⟩ slip, 18 % for pyramidal ⟨c + a⟩ and 3.5 % for {11.2} twinning.

This activation sequence (Fig. 11) will influences the behavior of the polycrystal at the local level (i.e. at the diffracting volume level). Then, it is interesting to see its impact on the different mechanical states of {hk.l} grain families. To illustrate this, the evolution of residual intergranular strains is shown in Fig. 12 for both longitudinal (loading direction) and transversal directions. When a polycrystalline aggregate is subjected to a tensile test in the elastic region, the lattice strains develop linearly with the load up to the micro-yielding point. There is a significant difference in the elastic response for each {hk.l} grain family due to the elastic anisotropy and the range of possible crystallographic orientations. Slip activity is initiated in plasticity regime in some grains similarly orientated. One can notice the accommodation of the imposed plastic deformation and these grains undergo less loads.

The neutron experiments results shown in Fig. 12 clearly highlight an anisotropic mechanical behavior of {hk.l} groups of grains.

According to the simulations, plasticity initiation begins with the yielding of $\{10.0\}_{//}$ grains at 260 MPa (corresponding to 0.24 % of total strain). Theses grains are favorably oriented for prismatic slip P⟨a⟩, the lowest-CRSS mechanism, correlated with a favorable Schmid factor (i.e. 0.5) for these orientations [4,6,67]. Indeed, the grains that activate the prismatic slip first and most easily are those which have their lattice crystalline $\vec{c}$-axis perpendicular to the loading direction. These grains undergo plastic deformation below the macroscopic yield stress (R_E = 280 MPa). It should be recalled that the outset of microplasticity does not cause

498 the macroscopic yield because slip activity is initiated in a small number of grains. As the
499 applied stress increases, $\{20.1\}_{//}$ orientation begins to shed load at 300 MPa. This can be
500 explained by the activation of pyramidal slip $\Pi_1\langle a\rangle$. The $\{10.1\}_{//}$ and $\{10.2\}_{//}$ orientated
501 grains yield at 330 MPa, reflecting the high activity of the basal slip (~ 45 % of activity
502 proportion).

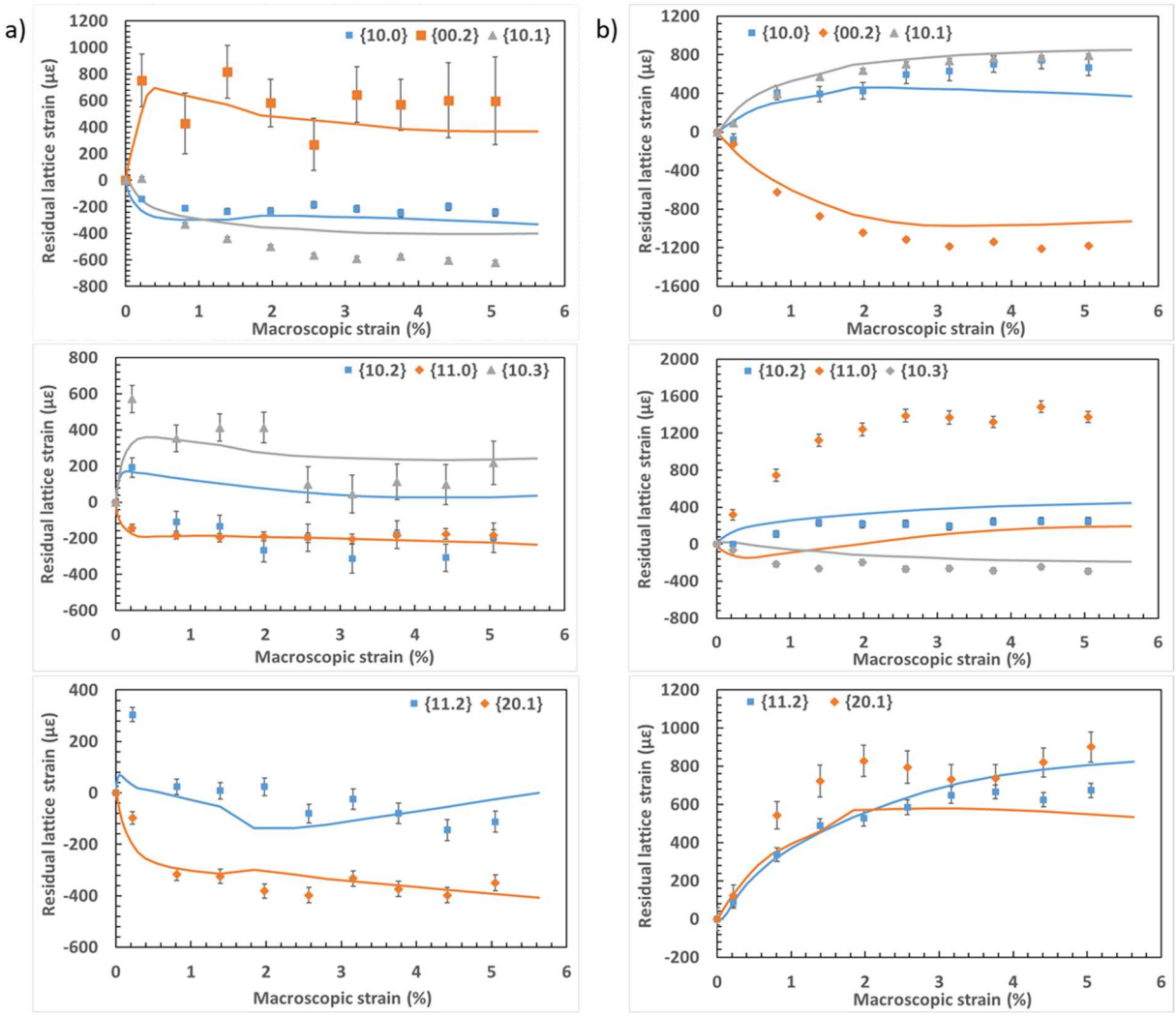

503

504 **Fig. 12**: Residual experimental (symbols) and predicted (lines) lattice strain evolution in both
505 (a) longitudinal and (b) transversal directions versus applied stress during neutron diffraction
506 experiments.

507 One can notice the linear deviation of the hardest $\{11.2\}_{//}$ grains (Fig. 12) with a change in
508 relative activity between prismatic P⟨a⟩ and basal B⟨a⟩ slips (Fig. 11). Other orientations such

509 as $\{10.3\}_{//}$ and $\{00.2\}_{//}$ yield only at 355 MPa with the activation of the pyramidal mode
510 $\Pi_1\langle c+a\rangle$ or $\{11.2\}$ twinning deformation. These $\{hk.l\}_{//}$ grains have the $\vec{c}$-axis nearly
511 aligned along the LD and they are poorly orientated for the soft $\langle a\rangle$ slip mechanism to be
512 activated. In the LD, the largest compressive residual strains are observed for $\{10.1\}_{//}$ and
513 $\{20.1\}_{//}$ grains (~ -620 με and ~ -399 με at 5 % of total strain, respectively). Similar
514 behaviors can be seen along $\{10.0\}_{//}$, $\{10.2\}_{//}$ and $\{11.0\}_{//}$ orientations, although the lattice
515 strains are relatively smaller: ~ -246 με, ~ -312 με and ~ -183 με, respectively. These
516 behaviors are well captured by the model except for $\{10.2\}_{//}$ orientation where a shift of 335
517 με can be noticed between the experimental and simulated results. As shown in Fig. 12.a, the
518 $\{00.2\}_{//}$ grain orientation develops significant tensile residual lattice strains (~ 760 με) during
519 the first 1 % of total strain. This indicates that the load is redistributed towards the plastically
520 harder grains like the $\{00.2\}_{//}$ ones after the initiation of plasticity. This phenomenon is
521 expected since all these grains are poorly orientated for the soft $\langle a\rangle$ slip mechanisms. A
522 similar behavior is observed for the $\{10.3\}_{//}$ grains orientation relatively close to the $\{00.2\}_{//}$
523 one, although the experimental lattice strains are relatively smaller: 570 με. This set of grains
524 is also unfavorable to $\langle a\rangle$ slips. Their residual strain evolution is well described by the
525 numerical simulations.

526 In the TD (Fig. 12.b), the model predicts the evolution of intergranular strains in the majority
527 of the {hk.l} orientations studied even if some discrepancies are observed. All $\{hk.l\}_{\perp}$ grains
528 present an opposite behavior to that observed in the longitudinal direction, highlighting the
529 Poisson effect. The residual lattice strains evolution of $\{11.0\}_{\perp}$ reflection is under-predicted.
530 A large gap of 450 με is observed between the experimental and simulated results, beyond 2.3
531 % of total strain. For $\{20.1\}_{\perp}$ grains, the model captures the tensile state, although the state is
532 underestimated by ~ 250 με at 3 % of total strain. Nevertheless, for the majority of

orientations, in particular: $\{10.0\}_{\perp}$, $\{00.2\}_{\perp}$, $\{10.1\}_{\perp}$, $\{10.2\}_{\perp}$, $\{10.3\}_{\perp}$ and $\{11.2\}_{\perp}$, the predictions are fairly accurate with the exception of the$\{11.0\}_{\perp}$ reflection. Therefore, one can only to conclude that the difference could not be attributed to a lack of description of the hardening. In our opinion, this difference could be explained by the presence of heterogeneities in the set of grains participating to this orientation or by the reverse plasticity when the material is subjected to reverse loading. The differences between model calculations and measurements are more pronounced than in the $\{hk.l\}_{//}$ grains. Similar observation has been made in previous studies [13,48].

4. 2 Synchrotron diffraction results

In contrast to neutron diffraction experiments, *in situ* synchrotron measurements have been performed during a continuous tensile test. Fig. 10.b shows the experimental and predicted bulk response. The simulated results describe with accuracy the elastic and plastic slopes up to 4 % macroscopic strain. The calculated Young's modulus of 107 GPa is very close to the experimental one of 109 ± 2 GPa. These values are consistent with those found in the neutron diffraction analysis. This proves that the model parameters allow to describe the elastic behavior of the material, suggesting that the elastic constants used in the modeling are quite reasonable with a well-described crystallographic texture. The yield stress is 240 MPa with the prismatic slip P⟨a⟩ as the main deformation mode (Fig. 13).

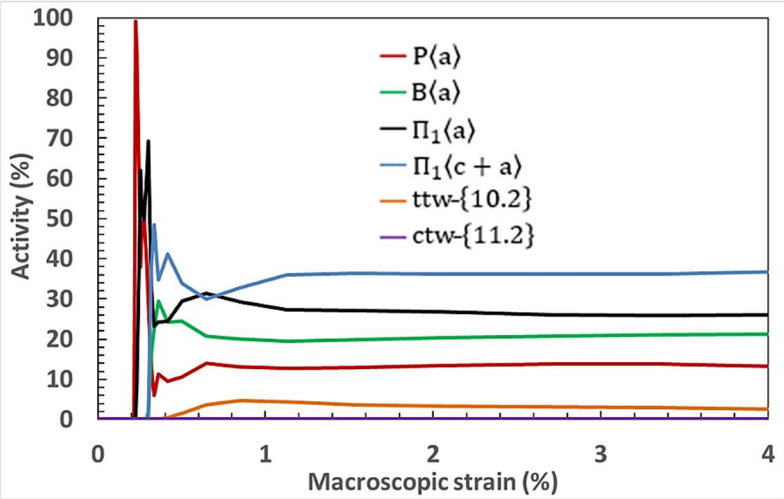

551

552 **Fig. 13**: Relative activities of the different active deformation modes for uniaxial tensile
553 loading during synchrotron diffraction experiments

554 Its initial CRSS value (110 MPa, see Table 3) is consistent with that found for N-sample and
555 more generally with α-titanium [64–68].

556 Concerning the prediction of lattice strain evolution, only the results obtained in the
557 longitudinal direction were retained. Indeed, for a given $\{\mathbf{hk.l}\}_{//}$ reflection, all diffracting
558 grains have the same orientation of the $\vec{\mathbf{c}}$-axis with respect to the tensile direction. They have
559 more-or-less the same deformation history and the Schmid factors for each deformation
560 system are the same for these grains. The grains which participate in the $\{hk.l\}_{\perp}$ reflection
561 have a wide range of crystallographic orientations with respect to the loading axis. In other
562 words, a rotation of a grain around an axis perpendicular to the loading direction highly
563 changes the stiffness in the tensile direction and, consequently, the strain and stress state in the
564 grain. The lattice strain of the diffracting grains, for the considered {hk.l} reflection, shows
565 large variation.

566 The mechanical response in the TD is very sensitive to the texture and the elastic strain
567 measured is thus the average over a set of diffracting grains with different strain history.
568 Many authors have already pointed out this problem [11,13,70,71]. This can explain the more

569 pronounced discrepancies noticed between calculations and measurements in the direction
570 perpendicular to the tensile axis in the section 4. 1. Moreover, the number of diffracting grains
571 in X-ray synchrotron experiments is weak as compared to neutron diffraction experiments due
572 to the reduced gauge volume. Therefore, the lattice strains determined with synchrotron X-ray
573 radiation are less representative of the polycrystal due to a smaller number of crystallites
574 contributing to the diffracting volume.

575 The comparison with the homogenization approach is then more problematic especially in the
576 TD. In the LD, this problem remains present but, for a given $\{\mathbf{hk.l}\}_{//}$ reflection, all the grains
577 have an identical lattice plane normal in a direction parallel to the tensile axis with a very
578 similar mechanical state for these grains in plasticity. The range of lattice strains for all grains
579 in the diffracting volume along the longitudinal direction is lower than the range of the strains
580 for the transverse direction within a given {hk.l} family. This compensates somehow the lack
581 of statistics met with the gauge volume. Therefore, the focus is made on the internal strain
582 evolution in the LD. The lattice strain evolution is reasonably predicted along LD (Fig. 14). In
583 the elastic regime, a linear evolution is observed whose slope depends on the grain family due
584 to the elastic anisotropy, each group of grains shows a more or less stiff behavior.

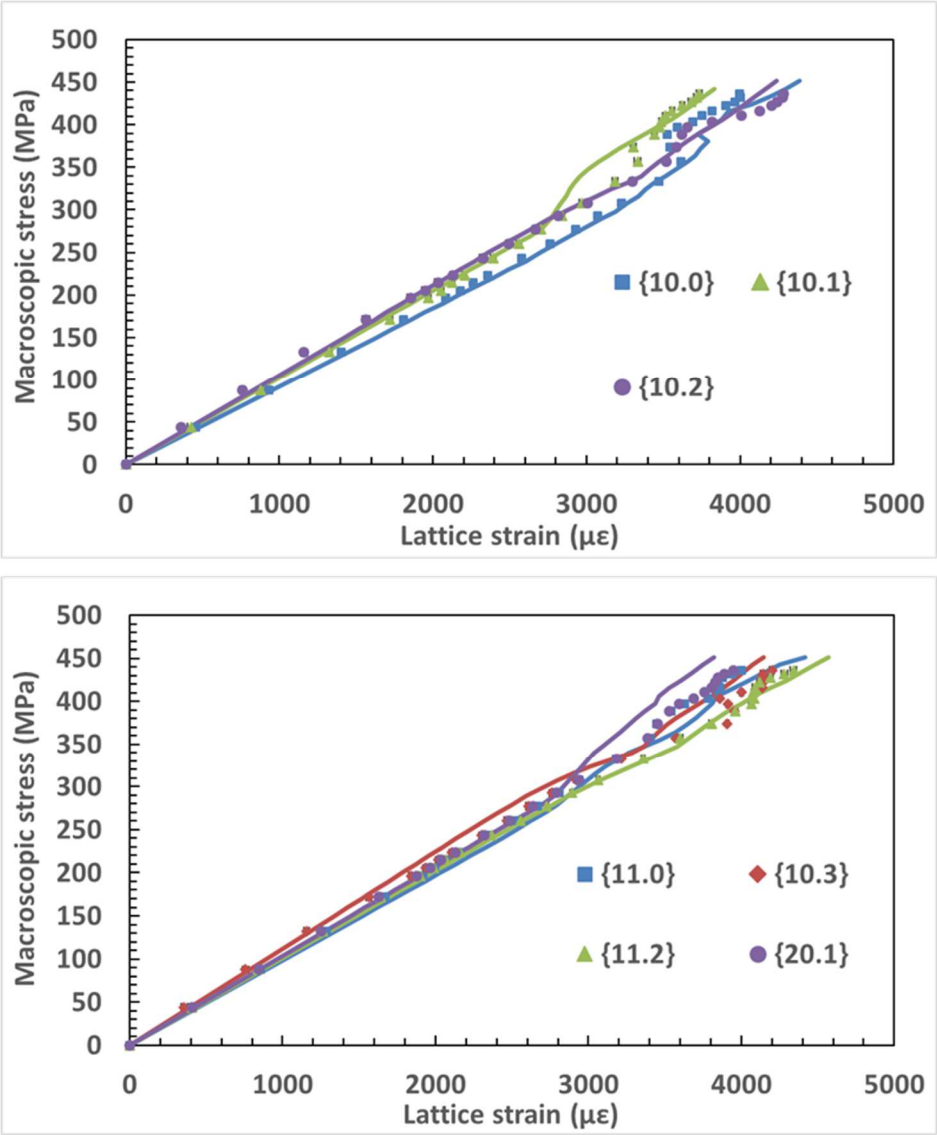

585

586 **Fig. 14**: Experimental (symbols) and predicted (lines) lattice strain evolution along LD for
587 tensile test during synchrotron diffraction experiments

588 For example, $\{\mathbf{10.0}\}_{//}$ grains family, which exhibit the most compliant behavior with the
589 lowest elasticity modulus $E_{hk.l}$ (Table 5), accumulate the largest elastic lattice strains as
590 compared to those met for $\{\mathbf{1.01}\}_{//}$ and $\{\mathbf{10.2}\}_{//}$ reflections. The elastic modulus $E_{hk.l}$ are
591 very well predicted by the model.

592 **Table 5:** Measured and predicted elastic modulus $E_{hk.l}$ (GPa) for different reflections $\{hk.l\}_{//}$

	{10.0}	**{10.1}**	**{10.2}**	**{11.0}**

Experimental	93 ± 0.8	103.2 ± 1	104.2 ± 1.8	97.8 ± 1.4
Model	92.2	102.5	105.8	98.6
	{10.3}	**{11.2}**	**{20.1}**	_
Experimental	113.6 ± 2	104 ± 1	100 ± 1.4	_
Model	112.3	103.8	101.6	_

593

594 In general, the simulations exhibit a reasonable agreement with the experiment in terms of
595 both trends and magnitudes. The relative activities of the deformation modes are plotted in
596 Fig. 13. The $\{10.0\}_{//}$ and $\{11.0\}_{//}$ grain families yield first at 240 MPa. Such micro-yielding
597 is correctly reproduced by the model, and it is clear that this first inflection is induced by the
598 activation of prismatic slip P⟨a⟩. At 260 MPa, the $\{20.1\}_{//}$ and $\{10.1\}_{//}$ grain families begins
599 to shed load due to the activation of pyramid slip $\Pi_1\langle a\rangle$. A third inflection taking place at 306
600 MPa is observed for the $\{10.2\}_{//}$ and $\{11.2\}_{//}$ orientations. This inflection is a result of the
601 activity of basal slip B⟨a⟩. A significant load partitioning takes place later in $\{10.3\}_{//}$ grains,
602 and is associated with the noteworthy activity of pyramidal $\Pi_1\langle c+a\rangle$. This slip mode
603 becomes very quickly the major slip system governing the material plasticity until 4 % of the
604 total strain (Fig. 13).

605 The effect of crystallographic texture difference between N- and S-samples is clearly visible
606 in the evolution of relative activities of the different active deformation systems. In the N-
607 sample, the majority of the grains have the $\vec{c}$-axis nearly perpendicular to the loading axis and
608 they are favorably oriented for the prismatic slip P⟨a⟩ while in the S-sample, the rolling
609 texture induces the significant activity of pyramidal $\Pi_1\langle c+a\rangle$ (see Fig. 11 and Fig. 13). At ~
610 365 MPa, the lattice strain relief in the $\{10.0\}_{//}$ grains is caused by the {10.2} tensile
611 twinning inducing a stress relaxation. This observation has been made in previous works [71–

612 73], and is well captured by the simulations. It is noted that {11.2} compressive twinning
613 during the deformation is almost negligible, which is consistent with the initial
614 crystallographic texture of the S-sample (Fig. 7).

615 For diffraction measurements, the residual strains usually show poorer agreement between
616 measurements and simulation results than the *in situ* strains measured under a mechanical
617 load. This can be explained by the fact that the model does not take into account slip activity
618 [70] or twinning-detwinning [74] one during unloading (i.e the reverse plasticity, when the
619 material is subjected to reverse loading, is not predicted by the model). The experimental
620 macroscopic stress-strain curves show actually a slight reverse plasticity during the unloads,
621 especially for large macroscopic strain values (see Fig. 10), for stress values close to zero.
622 Some discrepancies between the model predictions and the measurements could therefore be
623 expected. Despites this limitation, residual strain evolution is well described by the numerical
624 simulations for the majority of {hk.l} orientations along the LD and TD (see Fig. 12). The
625 observed discrepancies ($\{10.2\}_{//}, \{11.0\}_{\perp}$ for example) between the model predictions and the
626 measurements could be partially explained by this lack of description. On the other hand, the
627 main limitation of synchrotron is the small gauge volume resulting in a limited number of
628 diffracting grains for a given reflection and an exacerbated sensitivity of the results to spatial
629 heterogeneities. The comparison with a homogenization approach becomes then more
630 problematic. In our study, in order to overcome this problem, only longitudinal strains have
631 been analyzed and intensity of each diffraction ring has been integrated within ”cake shape”
632 sectors defined by $\beta \pm 10°$. The arithmetic mean values of the d-spacings were subsequently
633 calculated from the averaging of the symmetrically equivalent γ and $\gamma + 180°$ angles (see
634 section 2.3). Moreover, the ratios between the CRSS of the different deformation modes with
635 respect to the one of the P⟨a⟩ family are in agreement with the ranges identified with neutron
636 diffraction. These results are in accordance with those obtained, for example, by Barkia et al.

637 [67] by TEM (slip trace analysis) or Amouzou et al. [68] with an EVPSC model. The same
638 activation sequence combination has been used for these two experiments. Therefore, we can
639 deduce that the longitudinal lattice strains determined with synchrotron X-ray radiation are
640 representative due to a sufficient number of crystallites contributing to the diffracting volume
641 for the LD.

642 Nevertheless, due to the crystallographic texture, the activity rates for the different
643 deformation modes are not the same according to the samples of this study.

644 **5. Conclusion**

645 In this work, the evolution of lattice strains and texture under mechanical loading in α-Ti alloy
646 has been examined using two different techniques: neutron and X-ray synchrotron
647 diffractions. These results have been compared with the prediction of EPSC model and the
648 elastoplastic deformation has been studied at the different scales. The major conclusions are
649 summarized as below:

650 ➢ An extended EPSC model taking into account twin domain reorientation and
651 associated stress relaxation has been developed. On the basis of this study, the relative
652 activity of slip and twinning deformation modes occurring in the samples have been
653 determined and analyzed. By tuning the hardening coefficient and the initial CRSS, it
654 is shown that the model predictions, in terms of lattice strain evolution (8 and 7
655 different reflections for neutron and synchrotron diffraction, respectively) and
656 macroscopic stress-strain curves are in good agreement with the experimental data.
657 The lattice strain relief caused by the twinning is well captured by the simulations.
658 ➢ Our work highlights the strong crystallographic texture effect onto the deformations
659 mechanisms activation sequence of N- and S-samples. In the N-sample, the majority
660 of the grains have the $\vec{c}$-axis nearly perpendicular to the loading axis and they are

favorably oriented for the prismatic slip P⟨a⟩ (and for the tensile twinning $\{10.2\}\langle 10.\bar{1}\rangle$) while in the S-sample, the rolling texture induces the significant activity of pyramidal $\Pi_1\langle c+a\rangle$.

- X-ray synchrotron source offers fast rates of data acquisition (few seconds for X-rays and about 40 minutes for neutron diffraction in this work) enabling real time and *in situ* strain distribution measurements during continuous mechanical loading. Despite a small irradiated volume for X-rays, the inflections of {hk.l} orientations due to the slip or twinning deformation modes are relatively well reproduced by the model. This agreement is only obtained in the LD with intensity of each diffraction ring has been integrated within "cake shape" sectors defined by $\beta \pm 10°$. The arithmetic mean values of the d-spacings were calculated from the averaging of the symmetrically equivalent γ and $\gamma + 180°$ angles.
- The advantage of neutron diffraction techniques is notably related to a substantial and representative scattering volume of $4 \times 4 \times 4$ mm^3. Despite the fact that the model does not take into account slip activity or twinning-detwinning one during unloading, residual strain evolution is well described by the numerical simulations for the majority of {hk.l} orientations along LD and TD.
- The comparison between the extended EPSC model with *in situ* or *post mortem* characterization give the same trends: the ⟨a⟩ slip on prismatic planes is the easiest deformation mechanism. Pyramidal ⟨a⟩ slip is the second easiest and basal ⟨a⟩ slip the third. ⟨c + a⟩ slip is regarded as more difficult than ⟨a⟩ slip mechanisms which result in twinning to accommodate strain along the $\vec{c}$- axis.

Acknowledgements

685 The authors gratefully acknowledge the ISIS Neutron Facility and the ESRF scientific
686 committees for the allocated experimental days on ENGIN-X (experiment RB171006) and
687 GEM (experiment RB1890207), and ID15B (experiment ME1356) instruments, respectively.

688 **References**

689 [1] K. Wang, The use of titanium for medical applications in the USA, Mater. Sci. Eng. A.
690 213 (1996) 134–137. https://doi.org/10.1016/0921-5093(96)10243-4.

691 [2] H. Sibum, Titanium and titanium alloys - From raw material to semi-finished products,
692 Adv. Eng. Mater. 5 (2003) 393–398. https://doi.org/10.1002/adem.200310092.

693 [3] H.J. Rack, J.I. Qazi, Titanium alloys for biomedical applications, Mater. Sci. Eng. C.
694 26 (2006) 1269 – 1277. https://doi.org/10.1007/978-3-662-46836-4_8.

695 [4] P.G. Partridge, The crystallography and deformation modes of hexagonal close-packed
696 metals, Metall. Rev. 12 (1967) 169–194. https://doi.org/10.1179/mtlr.1967.12.1.169.

697 [5] A.A. Pochettino, N. Gannio, C.V. Edwards, R. Penelle, Texture and pyramidal slip in
698 Ti, Zr and their alloys, Scr. Metall. Mater. 27 (1992) 1859–1863.
699 https://doi.org/10.1016/0956-716X(92)90033-B.

700 [6] D.R. Chichili, K.T. Ramesh, K.J. Hemker, The high-strain-rate response of alpha-
701 titanium: Experiments, deformation mechanisms and modeling, Acta Mater. 46 (1998)
702 1025–1043. https://doi.org/10.1016/S1359-6454(97)00287-5.

703 [7] M.G. Glavicic, A.A. Salem, S.L. Semiatin, X-ray line-broadening analysis of
704 deformation mechanisms during rolling of commercial-purity titanium, Acta Mater. 52
705 (2004) 647–655. https://doi.org/10.1016/j.actamat.2003.10.025.

706 [8] J.L.W. Warwick, N.G. Jones, K.M. Rahman, D. Dye, Lattice strain evolution during
707 tensile and compressive loading of CP Ti, Acta Mater. 60 (2012) 6720–6731.

https://doi.org/10.1016/j.actamat.2012.08.042.

[9] D. Gloaguen, G. Oum, V. Legrand, J. Fajoui, S. Branchu, Experimental and theoretical studies of intergranular strain in an alpha titanium alloy during plastic deformation, Acta Mater. 61 (2013) 5779–5790. https://doi.org/10.1016/j.actamat.2013.06.022.

[10] J.R. Cho, D. Dye, K.T. Conlon, M.R. Daymond, R.C. Reed, Intergranular strain accumulation in a near-alpha titanium alloy during plastic deformation, Acta Mater. 50 (2002) 4847–4864. https://doi.org/10.1016/S1359-6454(02)00354-3.

[11] O. Muránsky, D.G. Carr, M.R. Barnett, E.C. Oliver, P. Šittner, Investigation of deformation mechanisms involved in the plasticity of AZ31 Mg alloy: In situ neutron diffraction and EPSC modelling, Mater. Sci. Eng. A. 496 (2008) 14–24. https://doi.org/10.1016/j.msea.2008.07.031.

[12] O. Muránsky, D.G. Carr, P. Šittner, E.C. Oliver, In situ neutron diffraction investigation of deformation twinning and pseudoelastic-like behaviour of extruded AZ31 magnesium alloy, Int. J. Plast. 25 (2009) 1107–1127. https://doi.org/10.1016/j.ijplas.2008.08.002.

[13] C.J. Neil, J.A. Wollmershauser, B. Clausen, C.N. Tomé, S.R. Agnew, Modeling lattice strain evolution at finite strains and experimental verification for copper and stainless steel using in situ neutron diffraction, Int. J. Plast. 26 (2010) 1772–1791. https://doi.org/10.1016/J.IJPLAS.2010.03.005.

[14] A. Baczmański, Y. Zhao, E. Gadalińska, L. Le Joncour, S. Wroński, C. Braham, B. Panicaud, M. François, T. Buslaps, K. Soloducha, Elastoplastic deformation and damage process in duplex stainless steels studied using synchrotron and neutron diffractions in comparison with a self-consistent model, Int. J. Plast. 81 (2016) 102–122. https://doi.org/10.1016/j.ijplas.2016.01.018.

732 [15] D. Gloaguen, B. Girault, J. Fajoui, V. Klosek, M.J. Moya, In situ lattice strains analysis
733 in titanium during a uniaxial tensile test, Mater. Sci. Eng. A. 662 (2016) 395–403.
734 https://doi.org/10.1016/j.msea.2016.03.089.

735 [16] J.L.W. Warwick, J. Coakley, S.L. Raghunathan, R.J. Talling, D. Dye, Effect of texture
736 on load partitioning in Ti-6Al-4V, Acta Mater. 60 (2012) 4117–4127.
737 https://doi.org/10.1016/j.actamat.2012.03.039.

738 [17] A.M. Stapleton, S.L. Raghunathan, I. Bantounas, H.J. Stone, T.C. Lindley, D. Dye,
739 Evolution of lattice strain in Ti-6Al-4V during tensile loading at room temperature,
740 Acta Mater. 56 (2008) 6186–6196. https://doi.org/10.1016/j.actamat.2008.08.030.

741 [18] S.L. Raghunathan, A.M. Stapleton, R.J. Dashwood, M. Jackson, D. Dye,
742 Micromechanics of Ti-10V-2Fe-3Al: In situ synchrotron characterisation and
743 modelling, Acta Mater. 55 (2007) 6861–6872.
744 https://doi.org/10.1016/j.actamat.2007.08.049.

745 [19] Y. Zhao, L. Le Joncour, A. Baczmański, E. Gadalińska, S. Wroński, B. Panicaud, M.
746 François, C. Braham, T. Buslaps, Stress distribution correlated with damage in duplex
747 stainless steel studied by synchrotron diffraction during plastic necking, Mater. Des.
748 113 (2017) 157–168. https://doi.org/10.1016/j.matdes.2016.10.014.

749 [20] A.C. Hannon, Results on disordered materials from the GEneral Materials
750 diffractometer, GEM, at ISIS, Nucl. Instruments Methods Phys. Res. A. 551 (2005)
751 88–107. https://doi.org/10.1016/j.nima.2005.07.053.

752 [21] W. Kockelmann, L.C. Chapon, P.G. Radaelli, Neutron texture analysis on GEM at
753 ISIS, Phys. B. 385–386 (2006) 639–643. https://doi.org/10.1016/j.physb.2006.06.091.

754 [22] L. Wu, A. Jain, D.W. Brown, G.M. Stoica, S.R. Agnew, B. Clausen, D.E. Fielden, P.K.

Liaw, Twinning – detwinning behavior during the strain-controlled low-cycle fatigue testing of a wrought magnesium alloy , ZK60A, Acta Mater. 56 (2008) 688–695. https://doi.org/10.1016/j.actamat.2007.10.030.

[23] J.R. Santisteban, M.R. Daymond, J.A. James, L. Edwards, ENGIN-X: A third-generation neutron strain scanner, J. Appl. Crystallogr. 39 (2006) 812–825. https://doi.org/10.1107/S0021889806042245.

[24] C.M. Moreton-Smith, S.D. Johnston, F.A. Akeroyd, Open GENIE-a generic multi-platform program for the analysis of neutron scattering data, J. Neutron Res. 4 (1996) 41–47. https://doi.org/10.1080/10238169608200066.

[25] J.E. Daniels, M. Drakopoulos, High-energy X-ray diffraction using the Pixium 4700 flat-panel detector, J. Synchrotron Radiat. 16 (2009) 463–468. https://doi.org/10.1107/S0909049509015519.

[26] A.P. Hammersley, S.O. Svensson, M. Hanfland, A.N. Fitch, D. Häusermann, Two-dimensional detector software: from real detector to idealised image or two-theta scan, High Press. Res. 14 (1996) 235–248. https://doi.org/10.1080/08957959608201408.

[27] G.K. Wertheim, M.A. Butler, K.W. West, D.N.E. Buchanan, Determination of the Gaussian and Lorentzian content of experimental line shapes, Rev. Sci. Instrum. 45 (1974) 1369–1371. https://doi.org/10.1063/1.1686503.

[28] P. Thompson, D.E. Cox, J.B. Hastings, Rietveld Refinement of Debye-Scherrer Synchrotron X-ray Data from Al2O3, J. Appl. Crystallogr. 20 (1982) 79–83. https://doi.org/10.1007/s003300101137.

[29] R.A. Young, D.B. Wiles, Profile shape functions in Rietveld refinements, J. Appl. Crystallogr. 15 (1982) 430–438. https://doi.org/10.1107/s002188988201231x.

778 [30] V. Hauk, Structural and Residual Stress Analysis by Nondestructive Methods, Elsevier,
779 Amsterdam, 1997. https://doi.org/10.1017/CBO9781107415324.004.

780 [31] E. Tenckhoff, Deformation mechanisms, texture, and anisotropy in zirconium and
781 zircaloy, ASTM Speci, ASTM Speci, Philadelphia, 1988.

782 [32] D.W. Brown, S.R. Agnew, M.A.M. Bourke, T.M. Holden, S.C. Vogel, C.N. Tomé,
783 Internal strain and texture evolution during deformation twinning in magnesium,
784 Mater. Sci. Eng. A. 399 (2005) 1–12. https://doi.org/10.1016/j.msea.2005.02.016.

785 [33] M.A. Gharghouri, C.G. Weatherly, J.D. Embury, J. Root, Study of the mechanical
786 properties of Mg-7.7at.% Al by in-situ neutron diffraction, Philos. Mag. A. 79 (1999)
787 1671–1695.

788 [34] E. Kröner, Zur plastischen verformung des vielkristalls, Acta Metall. 9 (1961) 155–
789 161.

790 [35] E. Kröner, Berechnung der elastischen Konstanten des Vielkristalls aus den Konstanten
791 des Einkristalls, Zeitschrift Für Phys. 151 (1958) 504–518.

792 [36] R. Hill, Continuum micro-mechanics of elastoplastic polycrystals, J. Mech. Phys.
793 Solids. 13 (1965) 89–101. https://doi.org/10.1016/0022-5096(65)90023-2.

794 [37] D. Gloaguen, T. Berchi, E. Girard, R. Guillén, Measurement and prediction of residual
795 stresses and crystallographic texture development in rolled Zircaloy-4 plates: X-ray
796 diffraction and the self-consistent model, Acta Mater. 55 (2007) 4369–4379.
797 https://doi.org/10.1016/j.actamat.2007.04.007.

798 [38] P. Lipinski, M. Berveiller, Elastoplasticity of micro-inhomogeneous metals at large
799 strains, Int. J. Plast. 5 (1989) 149–172. https://doi.org/10.1016/0749-6419(89)90027-2.

800 [39] P. Franciosi, M. Berveiller, A. Zaoui, Latent hardening in copper and aluminium single

crystals, Acta Metall. 28 (1980) 273–283. https://doi.org/10.1016/0001-6160(80)90162-5.

[40] J.-P. Lorrain, T. Ben-Zineb, F. Abed-Meraim, M. Berveiller, Ductility Loss Modelling for BCC Single Crystals, Int. J. Form. Process. 8 (2005) 135–158. https://doi.org/10.3166/ijfp.8.135-158.

[41] G. Franz, F. Abed-Meraim, J.P. Lorrain, T. Ben Zineb, X. Lemoine, M. Berveiller, Ellipticity loss analysis for tangent moduli deduced from a large strain elastic-plastic self-consistent model, Int. J. Plast. 25 (2009) 205–238. https://doi.org/10.1016/j.ijplas.2008.02.006.

[42] G. Proust, C.N. Tomé, G.C. Kaschner, Modeling texture, twinning and hardening evolution during deformation of hexagonal materials, Acta Mater. 55 (2007) 2137–2148. https://doi.org/10.1016/j.actamat.2006.11.017.

[43] I.J. Beyerlein, C.N. Tomé, A dislocation-based constitutive law for pure Zr including temperature effects, Int. J. Plast. 24 (2008) 867–895. https://doi.org/10.1016/j.ijplas.2007.07.017.

[44] K. Inal, R.K. Mishra, Crystal plasticity based numerical modelling of large strain deformation in hexagonal closed packed metals, Procedia IUTAM. 3 (2012) 239–273. https://doi.org/10.1016/j.piutam.2012.03.016.

[45] P. Van Houtte, Simulation of the rolling and shear texture of brass by the Taylor theory adapted for mechanical twinning, Acta Metall. 26 (1978) 591–604. https://doi.org/10.1016/0001-6160(78)90111-6.

[46] C.N. Tomé, R.A. Lebensohn, U.F. Kocks, A model for texture development dominated by deformation twinning: Application to zirconium alloys, Acta Metall. Mater. 39

824 (1991) 2667–2680. https://doi.org/10.1016/0956-7151(91)90083-D.

825 [47] R.A. Lebensohn, C.N. Tomé, A self-consistent anisotropic approach for the simulation
826 of plastic deformation and texture development of polycrystals: Application to
827 zirconium alloys, Acta Metall. Mater. 41 (1993) 2611–2624.
828 https://doi.org/10.1016/0956-7151(93)90130-K.

829 [48] B. Clausen, C.N. Tomé, D.W. Brown, S.R. Agnew, Reorientation and stress relaxation
830 due to twinning: Modeling and experimental characterization for Mg, Acta Mater. 56
831 (2008) 2456–2468. https://doi.org/10.1016/j.actamat.2008.01.057.

832 [49] L. Capolungo, I.J. Beyerlein, Nucleation and stability of twins in hcp metals, Phys.
833 Rev. B - Condens. Matter Mater. Phys. 78 (2008) 1–19.
834 https://doi.org/10.1103/PhysRevB.78.024117.

835 [50] L. Capolungo, P.E. Marshall, R.J. McCabe, I.J. Beyerlein, C.N. Tomé, Nucleation and
836 growth of twins in Zr: A statistical study, Acta Mater. 57 (2009) 6047–6056.
837 https://doi.org/10.1016/j.actamat.2009.08.030.

838 [51] L. Wang, Y. Yang, P. Eisenlohr, T.R. Bieler, M.A. Crimp, D.E. Mason, Twin
839 nucleation by slip transfer across grain boundaries in commercial purity titanium,
840 Metall. Mater. Trans. A Phys. Metall. Mater. Sci. 41 (2010) 421–430.
841 https://doi.org/10.1007/s11661-009-0097-6.

842 [52] S. Xu, M. Gong, Y. Jiang, C. Schuman, J.S. Lecomte, J. Wang, Secondary twin variant
843 selection in four types of double twins in titanium, Acta Mater. 152 (2018) 58–76.
844 https://doi.org/10.1016/j.actamat.2018.03.068.

845 [53] C.N. Tomé, R.A. Lebensohn, Code Visco-Plastic Self-Consistent (VPSC), in: U.S.
846 Dep. Energy Univ. Calif., 7c ed., Los Alamos National Laboratory, 2009.

847 [54] M. Wronski, M. Arul Kumar, L. Capolungo, R.J. McCabe, K. Wierzbanowski, C.N.
848 Tomé, Deformation behavior of CP-titanium: Experiment and crystal plasticity
849 modeling, Mater. Sci. Eng. A. 724 (2018) 289–297.
850 https://doi.org/10.1016/j.msea.2018.03.017.

851 [55] M. Pitteri, On the Kinematics of Mechanical Twinning in Crystals, in: Breadth Depth
852 Contin. Mech., 1986: pp. 671–703.

853 [56] H. Abdolvand, M.R. Daymond, C. Mareau, Incorporation of twinning into a crystal
854 plasticity finite element model: Evolution of lattice strains and texture in Zircaloy-2,
855 Int. J. Plast. 27 (2011) 1721–1738. https://doi.org/10.1016/j.ijplas.2011.04.005.

856 [57] L. Bao, C. Schuman, J.S. Lecomte, M.J. Philippe, X. Zhao, C. Esling, A study of twin
857 variant selection and twin growth in titanium, Adv. Eng. Mater. 13 (2011) 928–932.
858 https://doi.org/10.1002/adem.201100055.

859 [58] H. Qin, J.J. Jonas, H. Yu, N. Brodusch, R. Gauvin, X. Zhang, Initiation and
860 accommodation of primary twins in high-purity titanium, Acta Mater. 71 (2014) 293–
861 305. https://doi.org/10.1016/j.actamat.2014.03.025.

862 [59] R.A. Lebensohn, Modelling the role of local correlations in polycrystal plasticity using
863 viscoplastic self- consistent schemes, Model. Simul. Mater. Sci. Eng. Model. 7 (1999)
864 739–746.

865 [60] G. Proust, C.N. C.N.Tomé, G.C. Kaschner, Modeling texture, twinning and hardening
866 evolution during deformation of hexagonal materials, Acta Mater. 55 (2007) 2137–
867 2148. https://doi.org/10.1016/j.actamat.2006.11.017.

868 [61] G. Simmons, H. Wang, Single crystal elastic constants and calculated aggregate
869 properties, MIT Press. (1971). https://doi.org/10.1038/nrg2484.

870 [62] S. Zaefferer, A study of active deformation systems in titanium alloys: Dependence on,
871 Mater. Sci. Eng. A. 344 (2003) 20–30. https://doi.org/10.1016/S0921-5093(02)00421-
872 5.

873 [63] K. Sofinowski, M. Šmíd, S. van Petegem, S. Rahimi, T. Connolley, H. van
874 Swygenhoven, In situ characterization of work hardening and springback in grade 2 α-
875 titanium under tensile load, Acta Mater. 181 (2019) 87–98.
876 https://doi.org/10.1016/j.actamat.2019.09.039.

877 [64] A.T. Churchman, The slip modes of titanium and the effect of purity on their occurence
878 during tensile deformation of single crystals, Proc. R. Soc. London A. 226 (1954) 216–
879 226. https://doi.org/10.1098/rspa.1954.0250.

880 [65] A.A. Salem, S.R. Kalidindi, S.L. Semiatin, Strain hardening due to deformation
881 twinning in α-titanium: Constitutive relations and crystal-plasticity modeling, Acta
882 Mater. 53 (2005) 3495–3502. https://doi.org/10.1016/j.actamat.2005.04.014.

883 [66] B. Barkia, V. Doquet, E. Héripré, I. Guillot, Characterization and analysis of
884 deformation heterogeneities in commercial purity titanium, Mater. Charact. 108 (2015)
885 94–101. https://doi.org/10.1016/j.matchar.2015.09.001.

886 [67] B. Barkia, V. Doquet, J.P. Couzinié, I. Guillot, E. Héripré, In situ monitoring of the
887 deformation mechanisms in titanium with different oxygen contents, Mater. Sci. Eng.
888 A. 636 (2015) 91–102. https://doi.org/10.1016/j.msea.2015.03.044.

889 [68] K.E.K. Amouzou, T. Richeton, A. Roth, M.A. Lebyodkin, T.A. Lebedkina,
890 Micromechanical modeling of hardening mechanisms in commercially pure α-titanium
891 in tensile condition, Int. J. Plast. 80 (2016) 222–240.
892 https://doi.org/10.1016/j.ijplas.2015.09.008.

[69] G. Lütjering, J.C. Williams, Titanium, Second, Springer-Verlag, Berlin, 2007. https://doi.org/10.1007/978-3-540-73036-1.

[70] B. Clausen, T. Lorentzen, M.A.M. Bourke, M.R. Daymond, Lattice strain evolution during uniaxial tensile loading of stainless steel, 259 (1999) 17–24.

[71] F. Xu, R.A. Holt, M.R. Daymond, Modeling lattice strain evolution during uniaxial deformation of textured Zircaloy-2, Acta Mater. 56 (2008) 3672–3687. https://doi.org/10.1016/j.actamat.2008.04.019.

[72] F. Xu, R.A. Holt, M.R. Daymond, R.B. Rogge, E.C. Oliver, Development of internal strains in textured Zircaloy-2 during uni-axial deformation, Mater. Sci. Eng. A. 488 (2008) 172–185. https://doi.org/10.1016/j.msea.2007.11.018.

[73] C. Mareau, M.R. Daymond, Micromechanical modelling of twinning in polycrystalline materials: Application to magnesium, Int. J. Plast. 85 (2016) 156–171. https://doi.org/10.1016/j.ijplas.2016.07.007.

[74] L. Wang, G. Huang, Q. Quan, P. Bassani, E. Mostaed, M. Vedani, F. Pan, The effect of twinning and detwinning on the mechanical property of AZ31 extruded magnesium alloy during strain-path changes, Mater. Des. 63 (2014) 177–184. https://doi.org/10.1016/j.matdes.2014.05.056.